EFFECT OF DECELERATION ON LAMINAR SEPARATION BUBBLES ON SD7003 AIRFOILS

Wolfgang Dierl[†], **Rainer Hain** and **Christian J. Kähler**
Institute of Fluid Mechanics and Aerodynamics
University of the Bundeswehr Munich
Werner-Heisenberg-Weg 39, 85577 Neubiberg, Germany
[†]wolfgang.dierl@unibw.de

Serhiy Yarusevych
Department of Mechanical and Mechatronics Engineering
University of Waterloo
200 University Avenue West, Waterloo, Ontario, Canada, N2L 3G1
syarus@uwaterloo.ca

ABSTRACT

A detailed analysis of the spatio-temporal flow development of a laminar separation bubble (LSB) during deceleration of an airfoil model in a water towing tank from a constant chord Reynolds number to rest is conducted. Time-resolved Particle Image Velocimetry (PIV) was employed to perform quantitative flow field measurements over a range of decelerations. The focus was on the time dependent typology of the LSB and the dynamics of Kelvin-Helmholtz vortices. The results provide insight into the mechanism of LSB decay. The deceleration of the airfoil model results in a gradual shift of the separation point and the vortex roll-up location towards the leading edge which is in contrast to the trends expected for a quasi-steady decrease of the Reynolds number. For lower magnitudes of deceleration in the range considered here, the vortex shedding frequency decreases. However, at higher declarations, no distinctive vortex shedding can be observed. The effect of deceleration on the pressure gradient indicates that the deviation of the results from quasi-steady trends are attributed to significant inertial effects for the cases examined.

INTRODUCTION

Flights at aerodynamically low Reynolds numbers (Re $\leq$ 500,000), as typically for unmanned aerial vehicles flying in earth atmosphere or for future applications in challenging atmospheric conditions such as those encountered on Mars (Carreño Ruiz *et al.*, 2023), presents new challenges related to unsteady aerodynamics. These arise, for example, due to the high manoeuvrability of the flight vehicles or gusts. A formation of a laminar separation bubble (LSB) on the suction side of a lifting surface is common when airfoils are operated at low Re (Lissaman, 1983). An LSB forms when the laminar boundary layer separates from the surface due to an adverse pressure gradient, followed by a rapid transition in the separated shear layer, which leads to mean flow reattachment. A simplified model that has been shown to describe well the initial stages of the transition process within the separated shear layer is the amplification of minute disturbances driven by a Kelvin-Helmholtz (KH) instability. The KH instability is often preceeded by Tollmien-Schlichting (TS) waves inside the laminar boundary layer upstream of the separation point (Marxen *et al.*, 2013; Michelis *et al.*, 2018). This transient process eventually leads to a roll-up of the shear layer, resulting in a continuous vortex formation and shedding (Watmuff, 1999; Hain *et al.*, 2009). Numerous experiments and simulations analyzed this process (e.g. Istvan & Yarusevych, 2018; Ol *et al.*, 2005) and investigated the influence of several key parameters (e.g. angle of attack, Reynolds number and free-stream turbulence intensity) on the LSB (Hain *et al.*, 2009; Burgmann *et al.*, 2008; Kawai *et al.*, 2023). However, the investigations of unsteady inflow conditions are relatively rare, although these conditions typically occur in practical applications.

Experiments conducted by Gad-El-Hak *et al.* (1984) describe the influence of deceleration on the stability of a laminar boundary layer formed over an flat plated which is decelerated in a water towing tank. The results reveal an increasing instability of the boundary layer during deceleration. A theoretical analysis of a decelerated flat plate by Ishizawa & Kosugi (1994) suggests that the adverse pressure gradient arising due to flow deceleration, laminar boundary layer separation can take place. The separation point shifts upstream during the deceleration phase and terminates when the flat plate comes to rest. Lately, an increasing interest in transient inflow conditions, not limited to a canonical laminar flat plate boundary layer, can be noticed. For example, Polet *et al.* (2015) investigated flow over a decelerating airfoil in combination with a pitching motion to increase the understanding of perching. The influence of transient inflow conditions (change in free-stream velocity) on the spatio-temporal evolution of an LSB was investigated by Ellsworth & Mueller (1991) and Toppings & Yarusevych (2023) at relatively high and low rates of acceleration, respectively. At higher rates of acceleration and deceleration the behaviour of the LSB differs substantially from what would be expected due to a corresponding quasi-steady change in the Reynolds number (Ellsworth & Mueller, 1991), whereas Toppings & Yarusevych (2023) concluded that at lower rates of acceleration and deceleration the response of the LSB is largely quasi-steady. Both studies conducted the experiments in a wind tunnel with an accelerated/decelerated flow past a fixed airfoil model. As stated by Gad-El-Hak (1987), results of those experiments may differ from those conducted with an accelerated/decelerated body in a resting fluid (experiments in a water towing tank) on account of a non-inertial frame of reference (Fox & McDonald, 1985; Gledhill *et al.*, 2016).

The present work experimentally investigates the spatio-temporal development of an LSB over an airfoil decelerated from a constant velocity to rest in a water towing tank, as a model of a vehicle landing.

EXPERIMENTAL SETUP

All the experiments were performed in a water towing tank at the University of the Bundeswehr Munich. The test section is 8 m long, with a cross-section of $0.9 \times 0.9\,\mathrm{m}^2$. The water height during the experiments was 0.75 m. An SD7003 airfoil model with a chord length of $c = 250$ mm and a span of 750 mm was employed. The model was positioned vertically and equipped with a brush seal to seal the gap at the floor. To prevent distortions from the water surface and mitigate end effects, a glass end plate was installed, see Fig. 1a.

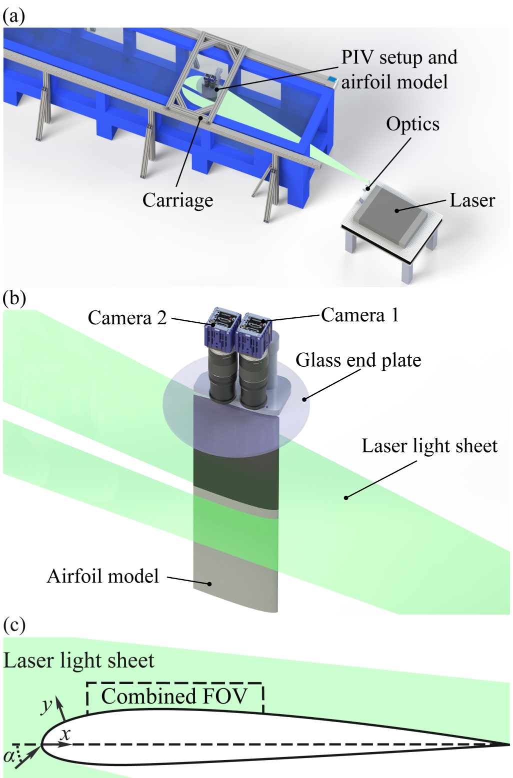

Figure 1. Experimental setup: (a) overview (b) wing model and PIV arrangement (c) combined Field of View (cFOV) and coordinate system definition.

The model was mounted at an angle of attack of $\alpha = 6°$ and was decelerated from a constant chord Reynolds number $\mathrm{Re}_c = 60{,}000$ to rest. Four decelerations d were considered. The corresponding non-dimensional deceleration parameter D_C is defined by

$$D_C = \frac{d \cdot c}{U_{\mathrm{init}}^2} \tag{1}$$

where U_{init} is the initial, steady state velocity. The considered values are listed in Table 1. The resulting velocity profiles for the four investigated decelerations are shown in Fig. 2.

Table 1. Case parameters

Case	d (m/s^2)	D_C	Re
A	−0.05	−0.22	60,000
B	−0.10	−0.43	60,000
C	−0.20	−0.87	60,000
D	−0.50	−2.17	60,000

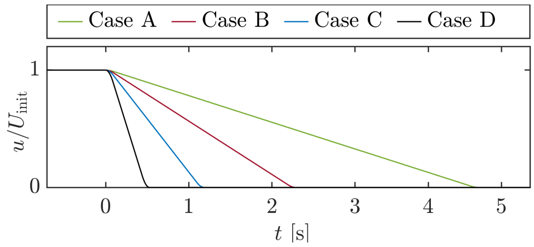

Figure 2. Velocity profiles.

Quantitative flow field measurements were performed using two-component time-resolved Particle Image Velocimetry (PIV) in a setup illustrated in Fig. 1. The water in the tank was seeded with 10 µm hollow glass spheres (LaVision), with a specific gravity of 1.1. The flow was illuminated by a Photonics DM150-532 DH Nd:YAG double-pulse laser. The laser light sheet was formed with a combination of spherical and cylindrical lenses and was coupled in at the front end of the water towing tank (Fig. 1a). Particle images were acquired by two cameras (LaVision Imager sCMOS) at 55 Hz in double-frame mode. Each camera was equipped with a Zeiss 100 mm fixed focal-length lens using a numerical aperture of 4. The camera sensors were cropped to $2560 \times 967\,\mathrm{px}^2$ each. The combined field of view (cFOV) at measurement position (Fig. 1b) from both cameras was $19 \times 89\,\mathrm{mm}^2$, with a magnification factor of 0.34. The vector fields were computed with LaVision DaVis 10 software using multi-pass cross-correlation with image deformation. The final interrogation window size was $32 \times 32\,\mathrm{px}^2$ with an overlap of 75 %. This results in a vector pitch of 0.16 mm. Table 2 presents essential PIV parameters. All results are presented in the wall-aligned coordinates (Fig. 1c).

A magnet band sensor (MBS) was used to measure the position of the model. The MBS data were recorded at 100 kHz simultaneously with the Q-switch signal from the laser, allowing to establish the temporal relation between the measured airfoil motion and velocity fields. Ten independent test runs, each yielding 550 measured velocity fields, were conducted per case. The distance travelled over which velocity measurements were conducted for each run was 1.50 m (or 6·c). Preliminary PIV measurements of the water movement subsequent to a measurement run were conducted. The time separation between each run was set to at least 300 s to reduce any adverse influence of residual perturbations from the previous run. At the selected time, based on a reference velocity of $v_{\mathrm{ref}} = 240\,\mathrm{mm/s}$ ($\widehat{=}\,\mathrm{Re}_c = 60{,}000$), the relative mean water movement velocity v_{m} and turbulence intensity level Tu_{240} in the towing tank dropped below 1.2 % and 0.05 %, respectively.

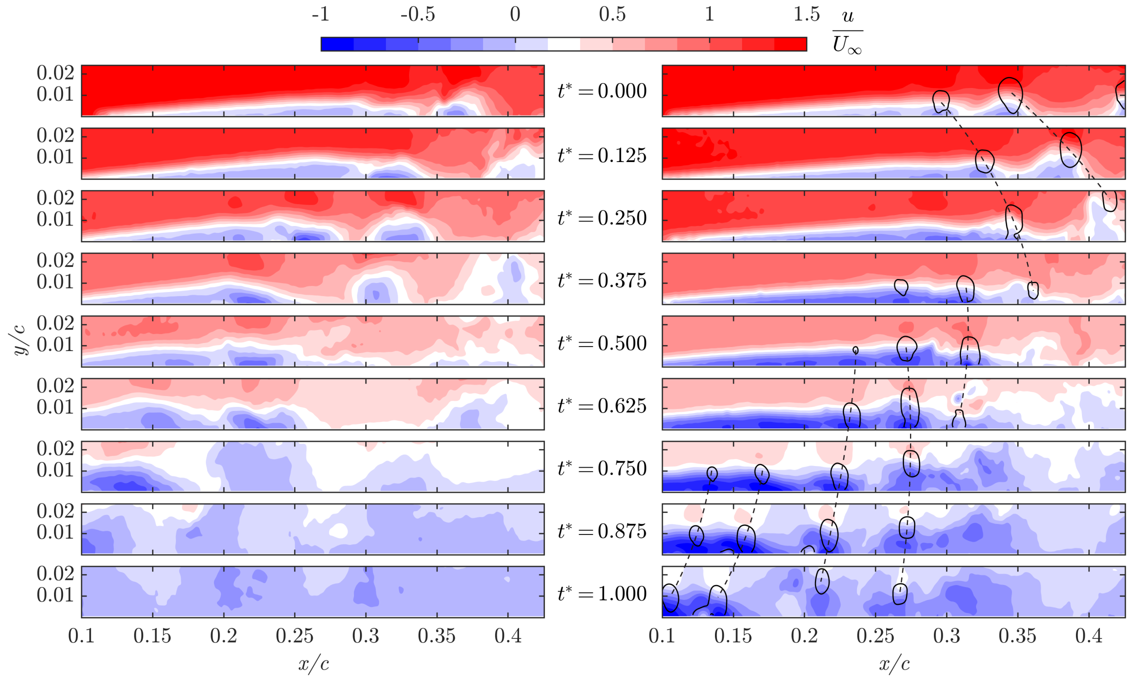

Figure 3. Temporal evolution of streamwise velocity contours for Case A (left) and Case D (right). Vortices for Case D are identified by λ_2-criterion contours ——, and the same structures are connected by - - -.

Table 2. PIV parameters

Parameters	
Light source	Photonics DM150-532 DH Nd:YAG
Light sheet thickness	≈ 2 mm
Laser pulse separation	1.2 ms
Seeding	LaVision 10 µm hollow glass spheres
Seeding specific gravity	1.1
Cameras	2× LaVision Imager sCMOS
Sensor size (cropped)	$2560 \times 967\,\mathrm{px}^2$
Combined field of view	$19 \times 89\,\mathrm{mm}^2$
Lens focal length	100 mm
Aperture $f_\#$	4
Magnification factor	0.34
Sampling frequency	55 Hz
Free-stream particle image displacement	≈ 17 px
Final interrogation window size	$32 \times 32\,\mathrm{px}^2$

Results

The response of an LSB flow field to flow deceleration is depicted in Fig. 3 for Case A and D (Table 1). The figure illustrates the temporal evolution of streamwise velocity contours by a sequence of nine consecutive time frames spaced by $\Delta t^* = 0.125$. The non-dimensional time

$$t^* = t \cdot \frac{d}{U_{\mathrm{init}}} \tag{2}$$

is introduced to account for different deceleration rates. For all the cases, the deceleration starts at $t^* = 0$, where $\mathrm{Re_c} = 60{,}000$, and the airfoil model comes to rest at $t^* = 1$. The results show that deceleration results in the upstream movement of both the separation point and the shear-layer roll-up location. At $t^* = 0$ the separation point is located at $x/c \approx 0.16$ and shifts out of the cFOV between $0.250 < t^* < 0.375$ for Case A and between $0.375 < t^* < 0.500$ for Case D. The roll-up location is defined as the location of the first detectable vortex identified by a continuous contour of the λ_2-criterion with a threshold set to $\lambda_2 = -20$. The results show that the shear-layer roll-up location starts to move upstream with the onset of deceleration ($t^* = 0$) from $x/c \approx 0.31$ and shifts out of the cFOV at $0.875 < t^* < 1$. The shear-layer roll-up location for Case D can be traced from $x/c \approx 0.31$ at $t^* = 0$ to $x/c \approx 0.11$ when the airfoil model comes to rest. The observed upstream shift of the vortex roll-up location during deceleration agrees well with the results of Ellsworth & Mueller (1991). The overall length of the recirculation region inside the LSB decreases over time for both cases, while its height and the magnitude of the reverse flow velocity increase over time. This implies that the time-scale for the separation point movement and the roll-up location movement in upstream direction differ. For Case A, a continuous vortex formation and shedding with a subsequent gradual drift of the vortices downstream can be observed up to $t^* \approx 0.625$. However, beyond this time shedding becomes difficult to identify and likely ceases, potentially when the shear parameter becomes too low for Kelvin-Helmholtz instability. As the transient time of Case D is shorter by a factor of 10 compared to Case A (see Fig. 2), the deceleration occurs over four to five vortex shedding cycles. Initially, the vortices drift downstream, followed by a stagnation at $t^* \approx 0.375$ and finally begin to advect towards the leading edge.

Figure 4 presents a comparison of ensemble average streamwise velocity fields over 10 deceleration runs for Cases A and D presented for several Reynolds numbers with corresponding mean LSBs obtained at corresponding steady state conditions. The results for the deceleration cases are smoothed over a 15-frame temporal window for Case A and three frames for Case D. It can be seen that both deceleration cases show notably different changes in flow development with Reynolds

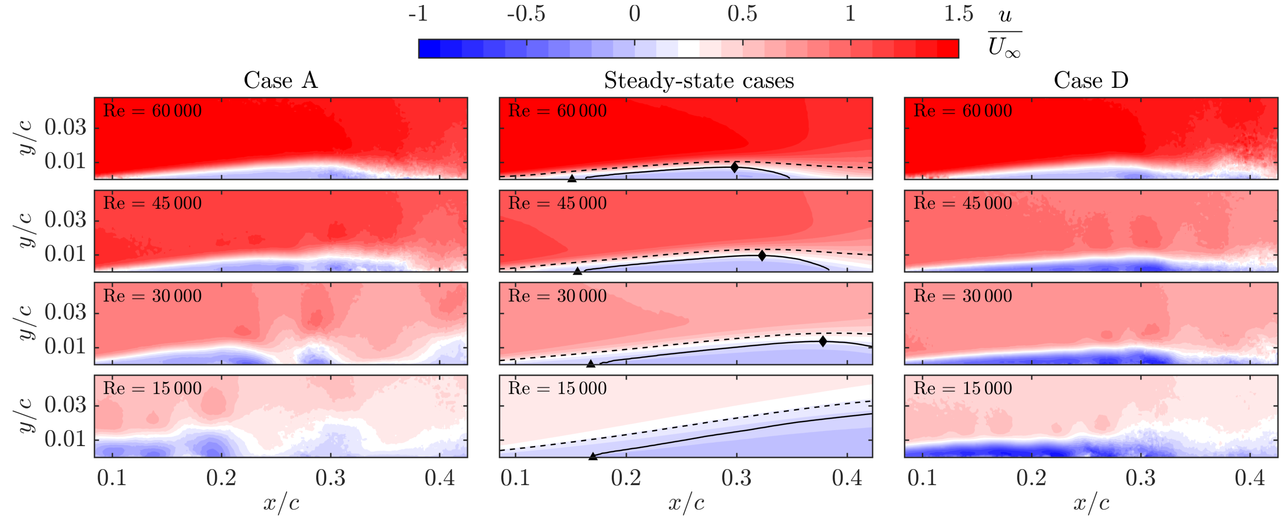

Figure 4. Ensemble averaged flow fields for Case A (left) and Case D (right) and mean flow fields at steady state conditions (middle). The displacement thickness - - -, dividing streamline ——, separation point ▲ and vortex roll-up location/transition point ♦ are shown for steady state conditions.

number compared to the steady state. Specifically, during the decrease of Re due to deceleration, there is a gradual movement of the separation point and LSB towards the leading edge for Cases A and D. This agrees with the findings of Ellsworth & Mueller (1991) for the decelerating free stream over a stationary airfoil. The observation is also similar to the analytically predicted shift of the separation point in a laminar flat plate boundary layer in response to the changes in adverse pressure gradient (APG) during incoming flow deceleration (Ishizawa & Kosugi, 1994). In contrast, LSBs corresponding to steady incoming flow show a delay of separation with decreasing Reynolds number. This is accompanied by a downstream shift in the location of the maximum bubble height with the overall lengthening of the LSB, leading to eventual bubble bursting and stall. For Case A and D, a continuous drift of the maximum bubble height towards the leading edge is observed. The observed flow development in response to deceleration contrasts that reported by Toppings & Yarusevych (2023), who observed essentially a quasi-steady response to substantially lower decelerations. It can thus be deduced that inertial effects are substantial for all the deceleration rates considered in the present investigation, which is discussed later in more detail.

Figure 5a and 5b illustrate the change of separation and vortex roll-up location for all the deceleration cases examined and steady state conditions over Re. Both figures emphasize that the upstream shift of the separation point and roll-up location during all the investigated deceleration cases is in contrast to the downstream shift of the corresponding values under steady state conditions. The location of the separation point with respect to Re (see Fig. 5a) is comparable between Cases A to D. However, the actual shift rate towards the leading edge in the temporal domain is lowest for Case A and constantly increases to Case D. A similar upstream shift is seen for the roll-up location (see Fig. 5b), albeit with higher variability. As the shift rates for the separation location are lower than those seen for the vortex roll-up location, the length of the LSB reduces during the deceleration phase, which can also be noted in the instantaneous snapshots in Fig. 3.

An analysis of the shedding process within the LSB indicates a strong dependency on the deceleration parameter. For Case A, persistent vortex shedding with a continuous decrease

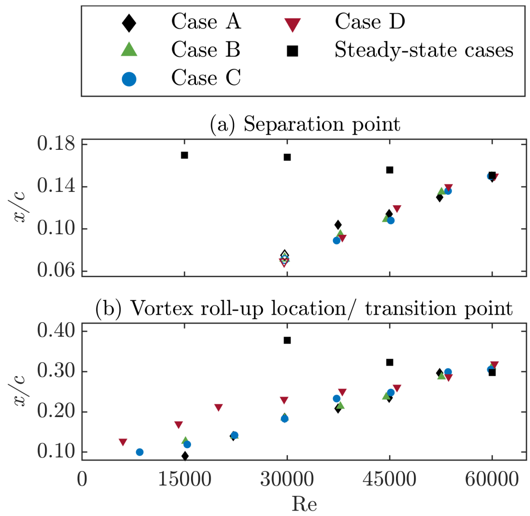

Figure 5. Separation point (a) and vortex roll-up location/transition point (b) for Cases A to D and steady state conditions. Empty markers indicate extrapolated values.

of the vortex shedding frequency was observed throughout the deceleration phase. The progressive decrease of the vortex shedding frequency qualitatively matches with the expectation at steady state flow conditions (Burgmann & Schröder, 2008). In order to characterize the vortex shedding frequency during the deceleration process, a wavelet analysis is performed based on a complex Morlet wavelet (Studer *et al.*, 2006), and the results are illustrated in Fig. 6a for Case A. As the shear-layer roll-up location constantly shifts upstream, a wavelet analysis of the wall-normal velocity fluctuations was conducted at five x/c locations. Figure 6b illustrates the gradual decrease of the vortex shedding frequency during deceleration based on ensemble averaged, maximum wavelet coefficient over ten runs. The frequency reduces from $f_s \approx 6.0\,\mathrm{Hz}$, with a corresponding chord-based Strouhal number of $\mathrm{St_c} \approx 6.8$ at $t^* = 0$, to $f_s \approx 2.0\,\mathrm{Hz}$ and $\mathrm{St_c} \approx 11.4$ at $t^* = 0.8$. The decrease in the shedding frequency during deceleration agrees within the experimental variability with that seen at decreasing Re under steady state conditions (identified by markers). Note that

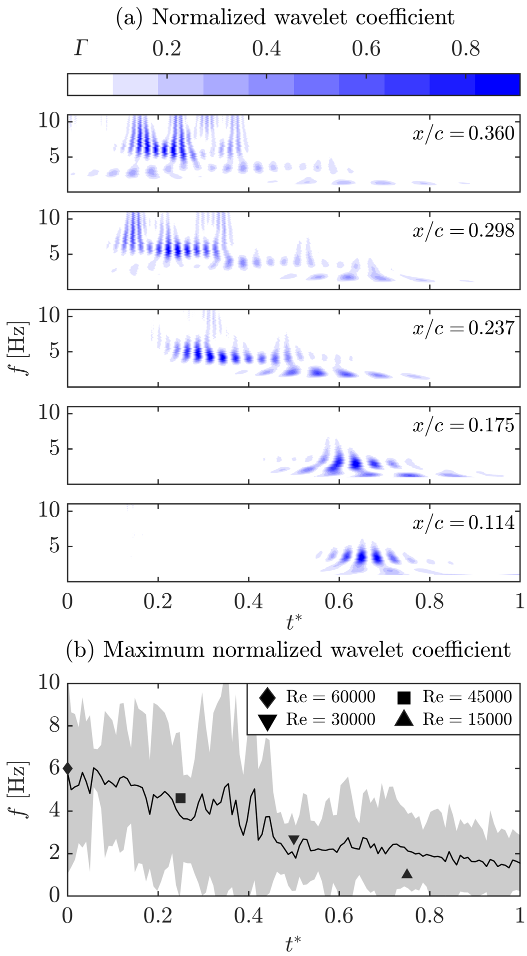

Figure 6. (a) Normalized wavelet coefficient (Γ) contours from wall-normal velocity fluctuations extracted at five x/c locations. (b) Vortex shedding frequency during deceleration for Case A (shaded area indicates $2\cdot\sigma$) based on ensemble averaged, maximum wavelet coefficient for Case A. Black filled markers indicate vortex shedding frequency at steady state Re.

it is not possible to determine the vortex shedding frequency for higher deceleration rates (Cases B to D) since the duration of deceleration phase is too short, resulting in an insufficient number of vortex shedding cycles for a reliable analysis.

Figure 7 illustrates the peak reverse flow velocity $u_{\min}$ in wall parallel direction during the deceleration phase for all the deceleration cases examined. To analyze $u_{\min}$, 20 % of the lowest (negative) values of wall parallel velocity vectors based on the ensemble averaged velocity fields for each case were considered. The peak reverse flow velocity for $t^* < 0$ (steady state conditions) fluctuates on average around the value of $-0.25\cdot U_{\mathrm{init}}$ for Cases A to D. This reverse flow velocity is lower by a factor of 2.5 compared to the mean minimal reverse flow velocity of the steady state LSB for Re $= 60{,}000$ (see Fig. 4). However, this is expected since only 20 % of the lowest (negative) values are considered in this analysis. When deceleration starts, values of $u_{\min}$ start to decrease. Both Case A and B saturate at $t^* \approx 0.25$ when $u_{\min} \approx 0.4\cdot U_{\mathrm{init}}$, followed by an increase past $t^* \approx 0.8$. Case C saturates at $t^* \approx 0.7$ when $u_{\min} \approx 0.75\cdot U_{\mathrm{init}}$, followed by an increase past $t^* \approx 0.9$. A consistent decrease of $u_{\min}$ is observed for Case D, reaching the minimum $u_{\min} \approx 1.0\cdot U_{\mathrm{init}}$ at $t^* = 1$ when the airfoil model comes to rest.

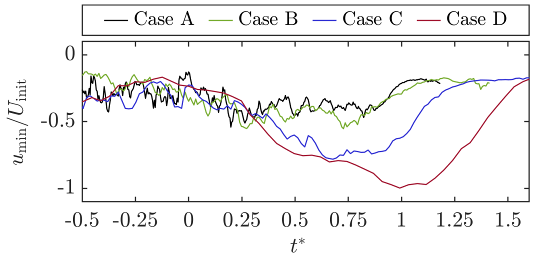

Figure 7. Ensemble averaged peak reverse flow velocity.

The difference of $u_{\min}$ between the Cases A and B and the Cases C and D indicates that there is an significant influence of the deceleration on this value. As the plots of Case A and B are similar, this indicates that a new equilibrium in the flow is established, whereby the magnitude of deceleration has a minor effect. For Case C and particularly Case D the magnitude of deceleration has a more pronounced effect on the transient flow development.

As suggested by Toppings & Yarusevych (2023), a modified version of the unsteady Bernoulli equation can be applied under certain assumptions to estimate the influence of acceleration and deceleration on the wall-parallel component of the pressure gradient. However, when the airfoil model is decelerated the coordinate-system fixed to the airfoil model is a non-inertial frame of reference. Thus an additional term for the translational deceleration $\mathrm{d}u_\infty/\mathrm{d}t$ of the airfoil model has to be considered (Fox & McDonald, 1985; Gledhill *et al.*, 2016), where u_∞ corresponds to the instantaneous towing velocity. Equation 3 is based on the suggestions of Toppings & Yarusevych (2023), extended for $\mathrm{d}u_\infty/\mathrm{d}t$:

$$\frac{\partial p}{\partial x} = -\rho\left(\frac{\partial u_{\mathrm{e}}}{\partial t} + u_{\mathrm{e}}\frac{\partial u_{\mathrm{e}}}{\partial x} + \frac{\mathrm{d}u_\infty}{\mathrm{d}t}\right) \tag{3}$$

where u_{e} is the local maximum edge velocity along x/c outside of the boundary layer. To calculate the actual temporal deceleration at the boundary layer edge, $\partial u_{\mathrm{e}}/\partial t$ has to be corrected by adding $\mathrm{d}u_\infty/\mathrm{d}t$. Figure 8 illustrates spatially averaged convective ($u_{\mathrm{e}}\cdot\partial u_{\mathrm{e}}/\partial x$) and temporal ($\partial u_{\mathrm{e}}/\partial t$) decelerations at the boundary layer edge within $0.1 < x/c < 0.15$ as well as $\mathrm{d}u_\infty/\mathrm{d}t$ and the sum of ($\partial u_{\mathrm{e}}/\partial t + \mathrm{d}u_\infty/\mathrm{d}t$). The results are presented until $t^* = 0.5$, at which time the transition location enters the spatial range considered for the estimation of the presented parameters (see Fig. 3 and Fig. 5b), and the assumptions for Eq. 3 no longer apply. The results show the expected progressive increase in the temporal edge velocity deceleration rate$\partial u_{\mathrm{e}}/\partial t$, accompanying the increase in the model deceleration rate $\mathrm{d}u_\infty/\mathrm{d}t$ from Case A to D. At the same time, with increased model deceleration rates, the effect of non-inertial correction becomes progressively significant, as seen in the increased magnitude of ($\partial u_{\mathrm{e}}/\partial t + \mathrm{d}u_\infty/\mathrm{d}t$). On the other hand, the convective acceleration term is comparable across the four deceleration cases, and as expected decreases in magnitude at the onset of deceleration due to the decrease of the local edge velocity. Consequently, for all the cases, the corrected temporal acceleration becomes significant during the deceleration process, and the significance of the associated influence on the global pressure gradient increases with increasing inertial effects from Case A to Case D. The associated progressive strengthening of the adverse pressure gradient (Eq.3) results in pronounced changes in the flow development compared to steady-state cases. Further, the results point to the importance of the correction for the model deceleration.

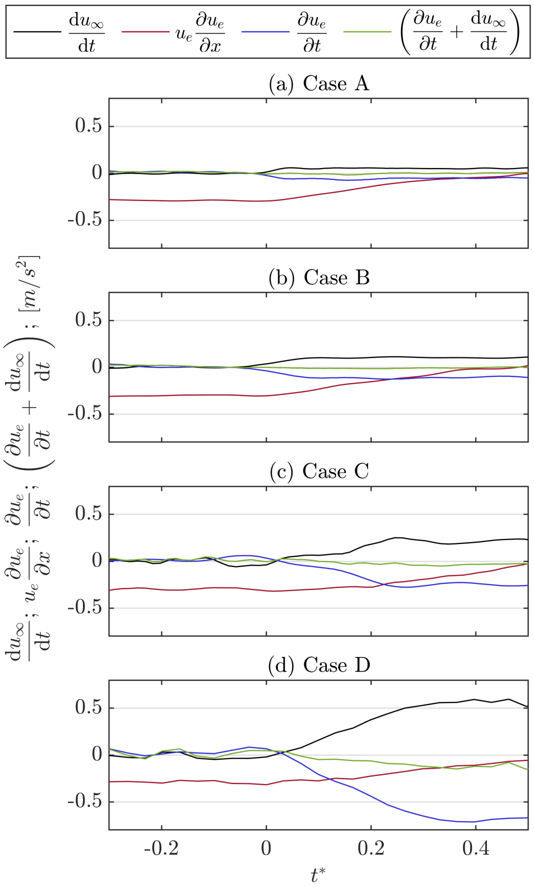

Figure 8. Comparison of acceleration terms for Cases A to D.

CONCLUSION

An experimental analysis of the flow on the suction side of an SD7003 airfoil model decelerated from a constant chord Reynolds number of 60,000 to rest was performed. PIV measurements were conducted to evaluate the effect of the airfoil model deceleration on the flow development. The results show that the separation point and the transition location shift towards the leading edge during deceleration which is in contrast to a quasi-steady change in Re. A wavelet analysis showed that the vortex shedding frequency gradually decreases during the deceleration phase before vortex shedding ceases at lower velocities. Analysing different contributions to the global pressure gradient reveals the significant influence of deceleration rates for all the cases the cases examined, and the importance of inertial corrections in towing tank experiments.

ACKNOWLEDGEMENT

The authors gratefully acknowledge the financial support of the German Research Foundation (DFG) for this project (Analysis of the transition process around laminar separation bubbles (LSB's) in a towing tank using time-resolved 3D particle tracking techniques, project number 422177304).

REFERENCES

Burgmann, S., Dannemann, J. & Schröder, W. 2008 Time-resolved and volumetric PIV measurements of a transitional separation bubble on an SD7003 airfoil. *Experiments in Fluids* **44** (4), 609–622.

Burgmann, S. & Schröder, W. 2008 Investigation of the vortex induced unsteadiness of a separation bubble via time-resolved and scanning PIV measurements. *Experiments in Fluids* **45** (4), 675–691.

Carreño Ruiz, M., Renzulli, L. & D'Ambrosio, D. 2023 Airfoil optimization for rotors operating in the ultra-low Reynolds number regime. *Physics of Fluids* **35** (10), 103603.

Ellsworth, R. H. & Mueller, T. J. 1991 Airfoil boundary layer measurements at low Re in an accelerating flow from a nonzero velocity. *Experiments in Fluids* **11** (6), 368–374.

Fox, R.W. & McDonald, A.T. 1985 *Introduction to Fluid Mechanics*. Wiley.

Gad-El-Hak, M. 1987 The water towing tank as an experimental facility. *Experiments in Fluids* **5**, 289–297.

Gad-El-Hak, M., Davis, S. H., Mcmurray, J. T. & Orszag, S. A. 1984 On the stability of the decelerating laminar boundary layer. *Journal of Fluid Mechanics* **138**, 297—-323.

Gledhill, I. M. A., Roohani, H., Forsberg, K., Eliasson, P., Skews, B. W. & Nordström, J. 2016 Theoretical treatment of fluid flow for accelerating bodies. *Theoretical and Computational Fluid Dynamics* **30**, 449–467.

Hain, R., Kähler, C. J. & Radespiel, R. 2009 Dynamics of laminar separation bubbles at low-Reynolds-number aerofoils. *Journal of Fluid Mechanics* **630**, 129–153.

Ishizawa, S. & Kosugi, S. 1994 Theoretical analysis for unsteady boundary layer on a linearly retarded semi-infinite flat plate. *JSME International Journal Series B* **37** (4), 795–805.

Istvan, M. S. & Yarusevych, S. 2018 Effects of free-stream turbulence intensity on transition in a laminar separation bubble formed over an airfoil. *Experiments in Fluids* **59** (3), 289.

Kawai, S., Asada, K. & Oyama, A. 2023 Freestream turbulence effects in Large-Eddy Simulations of laminar separation bubble. *Journal of Aircraft* **60** (5), 1721–1727.

Lissaman, P. B. S. 1983 Low-Reynolds-Number Airfoils. *Annual Review of Fluid Mechanics* **15** (1), 223–239.

Marxen, O., Lang, M. & Rist, U. 2013 Vortex formation and vortex breakup in a laminar separation bubble. *Journal of Fluid Mechanics* **728**, 58–90.

Michelis, T., Yarusevych, S. & Kotsonis, M. 2018 On the origin of spanwise vortex deformations in laminar separation bubbles. *Journal of Fluid Mechanics* **841**, 81–108.

Ol, M. V., McCauliffe, B., Hanff, E., Scholz, U. & Kähler, C. J. 2005 Comparison of laminar separation bubble measurements on a low reynolds number airfoil in three facilities. In *35th AIAA Fluid Dynamics Conference and Exhibit*, p. 483. Reston, Virigina: American Institute of Aeronautics and Astronautics.

Polet, D. T., Rival, D. E. & Weymouth, G. D. 2015 Unsteady dynamics of rapid perching manoeuvres. *Journal of Fluid Mechanics* **767**, 323–341.

Studer, G., Arnal, G., Houdeville, R. & Seraudie, A. 2006 Laminar–turbulent transition in oscillating boundary layer: experimental and numerical analysis using continuous wavelet transform. *Experiments in Fluids* **41**, 685–698.

Toppings, C. & Yarusevych, S. 2023 Transient dynamics of laminar separation bubble formation and bursting. *Experiments in Fluids* **64**, 57.

Watmuff, J. H. 1999 Evolution of a wave packet into vortex loops in a laminar separation bubble. *Journal of Fluid Mechanics* **397**, 119–169.